Acta Materialia 241 (2022) 118419

Contents lists available at ScienceDirect

Acta Materialia

journal homepage: www.elsevier.com/locate/actamat

Full length article

Phase decomposition in nanoporous Au-Pt

Maowen Liu[a,b,*], Jörg Weissmüller[a,b]

[a] Institute of Materials Mechanics, Helmholtz-Zentrum Hereon, Geesthacht, Germany
[b] Institute of Materials Physics and Technology, Hamburg University of Technology, Hamburg, Germany

ARTICLE INFO

Article history:
Received 5 August 2022
Revised 29 September 2022
Accepted 4 October 2022
Available online 8 October 2022

Keywords:
Nanoporous Au-Pt
Dealloying
Phase decomposition
Coarsening
Surface segregation

ABSTRACT

This study explores microstructure and phase decomposition in nanoporous Au-Pt made by dealloying. The starting alloy, $Ag_{75}Au_{12.5}Pt_{12.5}$, forms a uniform solid solution. Removing the Ag by dealloying at room temperature forms nanoporous equimolar Au-Pt with a ligament size as small as 4 nm. That alloy's composition is in the Au-Pt phase diagram's regime of spinodal instability. Surprisingly, in view of the instability and of the substantial atomic rearrangements accompanying dealloying, X-ray diffraction and transmission electron microscopy reveal a homogeneous single-phase state in the bulk of the nanoporous material. This can be traced back to enrichment of Pt at the surface, which depletes the bulk in Pt. The Pt-depleted bulk is in the metastable region of the alloy phase diagram, between the binodal and the spinodal. Annealing prompts curvature-driven coarsening by diffusion, diminishing the number of sites for Pt surface segregation. The ensuing enrichment of the bulk in Pt is accompanied by the formation first of crystallographically coherent, Pt-rich regions and later of semi-coherent regions of the Pt-rich phase. The morphology of the coherent regions is compatible with spinodal decomposition. Yet, the microstructure evolution pathway is nonstandard, since decomposition here concurs with rapid coarsening of the porous microstructure. Among the prospect of the nanoporous alloy are its high kinetic stability and the opportunity to tune the surface composition through the annealing temperature.

1. Introduction

Dealloying forms porous materials by nanoscale self organization during the selective removal of one component from a solid solution, typically by corrosion in aqueous media and at room temperature [1–3]. Nanoporous (np) gold is a prototypical object of study in this field. Standard preparation protocols result in ligament sizes in the order of 20–40 nm [4–6]. Alloying with Pt has been found to achieve much smaller ligament sizes, down to around 4 nm [6–10]. Furthermore, np Au-Pt alloys also exhibit a substantially enhanced stability against coarsening at elevated temperatures. Both observations have a natural explanation in the low surface diffusivity of Pt. As many interesting properties of nanoporous metals depend on a small ligament size, the reduced size and enhanced stability make np Au-Pt alloys highly attractive in the field.

Making np Au-Pt by dealloying involves the removal of Ag from a Ag-rich ternary solid solution. Consider specifically $Ag_{75}(Au_{0.5}Pt_{0.5})_{25}$. That solution is miscible down to near room temperature [11] and can be homogenized to form a single-phase state. Yet, when Ag is removed, the resulting $Au_{50}Pt_{50}$ is within the binary system's miscibility gap [12]. By virtue of its composition, it is even unstable with respect to spinodal decomposition [13]. In other words, the dealloying process' nanostructure formation involves not only the classic repartition of (1) the remaining metal atoms and (2) the vacancies (generated by dissolving the sacrificial component) into solid phase and pore space. Instead, it can also react to a thermodynamic driving force for unmixing the two remaining metallic elements. This is exemplified by phase separation during dealloying of Cu-Mn-Fe [14]. Yet, as dissolution rates can reach ~ 1 atomic monolayer per ms [15] at room temperature, dealloying is a process very far from equilibrium. It is then not obvious whether and in how far the elemental distribution in as-dealloyed nanoporous Au-Pt is affected by the miscibility gap.

Besides the question as to the microstructure generated by dealloying, the microstructure evolution of the porous material during coarsening is also not obvious. To start out with, geometric confinement may affect spinodal processes [16–18]. As bulk diffusion is suppressed and surface diffusion dominant at low annealing temperature, the unmixing of the bulk may be mediated by diffusion along a migrating surface, somewhat reminiscent of

* Corresponding author at: Institute of Materials Mechanics, Helmholtz-Zentrum Hereon, Geesthacht, Germany.
E-mail address: Maowen.Liu@hereon.de (M. Liu).

https://doi.org/10.1016/j.actamat.2022.118419

diffusion-induced grain boundary migration [19,20]. That decomposition pathway may have as yet unknown consequences for the kinetics and the resulting microstructure. Furthermore, the two nonequilibrium processes of coarsening and unmixing – each with its distinct driving force – will concur, again with nonobvious consequences for the microstructure evolution. Lastly, the extremely high number of surfaces implies that surface segregation can significantly affect the distribution of the elements at any given structure size.

Au-Pt nanostructures are of interest beyond nanoporous materials, specifically in the field of catalysis [7,9,21–23]. Surprisingly, related studies by X-ray diffraction do not reveal the expected two-phase structure of the immiscible system. Instead, diffractograms exhibit a single set of face-centered cubic (fcc) reflections [8,9,24,25]. It remains to be explored, why the two-phase state that is suggested by the alloy phase diagram is not reflected in the diffraction data of the as-prepared material. Regarding the microstructure evolution in nanostructured Au-Pt as the system evolves towards equilibrium during annealing and coarsening, few investigations have been reported. At elevated temperatures, phase separation at grain boundaries was identified in nanocrystalline Pt-Au [26]. In np Au-Pt, depletion of the surface in Pt after annealing in reductive environment was detected [27–29]. Nonetheless, a comprehensive understanding of the microstructure evolution in nanoscale Au-Pt is missing.

In this study, we report phase and composition analysis by analytic transmission electron microscopy (TEM), X-ray diffraction, and cyclic voltammetry that explore the microstructure of as-prepared np Au-Pt and its evolution during annealing.

2. Procedures

Nanoporous Au-Pt specimens were prepared following the procedure in reference [8]. $Ag_{75}(Au_{0.5}Pt_{0.5})_{25}$ (atom percent) wires with the diameter of 0.2 mm (ChemPUR Feinchemikalien und Forschungsbedarf GmbH, Germany) were annealed at 950 °C for 72 h followed by water quenching. The high-temperature and long-time annealing enabled the formation of homogeneous Ag-Au-Pt solid solution according to the phase diagram [11]. The master alloy was then dealloyed in 1 M $HClO_4$ solution, using a pseudo Ag/AgCl reference electrode at a potential of 0.8 V (1.315 V versus the reversible hydrogen electrode). Subsequently, the electrolyte was exchanged against fresh one, and 50 potential cycles ranging from -0.45 to 1.1 V at a scan rate of 5 mV/s were performed. This procedure was executed in order to remove superficial oxygen species. The specimens were then immersed in ultrapure water for one day and subsequently dried at room temperature.

Specimens were isothermally annealed in Ar (99.998 vol.% purity) flow at various temperatures for 1 h. For cooling, they were moved into the oven's room-temperature zone. The annealing treatment at each of the individual temperature steps started with a fresh, as-dealloyed sample.

The specimens for TEM observation were crushed to powders and then dispersed on lacey carbon film supported by Cu grids. The brittle nanostructure enables crushing the nanoporous specimens by gentle pressure. The microstructure and element distribution of the specimens were investigated using a FEI Talos F200X TEM equipped with a high-brightness Schottky field emission gun and four silicon drift detectors for energy dispersive X-ray spectroscopy (EDS). The high-angle annular dark-field (HAADF) images and EDS maps for the annealed specimens were acquired using an accelerating voltage of 200 kV and a probe current of 1 nA. For the as-dealloyed specimen consisting of extremely small ligaments, the HAADF images were obtained using an accelerating voltage of 200 kV and a current of 50 pA to improve the resolution, and the EDS maps were achieved using an accelerating voltage of 80 kV and a current of 1 nA to minimize beam damage. Spectrum images with a typical resolution of 512×512 pixels were acquired, and the dwell time for each pixel was 20 μs. Total acquisition time for each spectrum image was 1800 s. Those images were deconvoluted pixel-by-pixel before map construction, and L lines for Au, Pt and Ag were used for quantitative analysis.

Powders for X-ray diffraction were obtained using the same method with those for TEM observation. Powder diffraction measurements used a $\theta - \theta$ diffractometer (Bruker D8 Advance) in Bragg-Brentano geometry with Ni-filtered Cu $K\alpha$ radiation and a

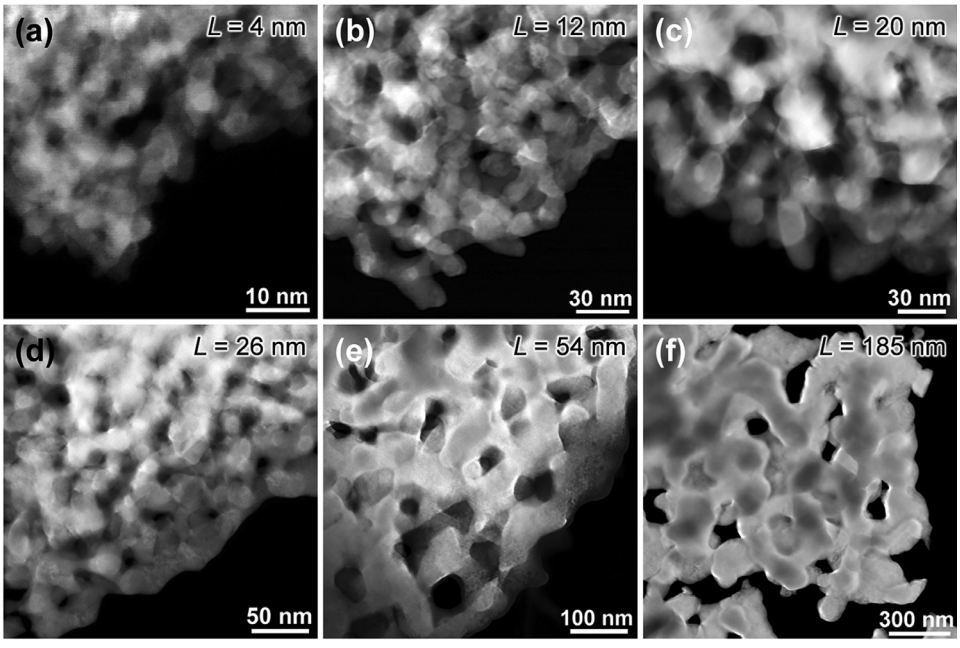

Fig. 1. Microstructure of (a) as-dealloyed and (b-f) isothermally annealed nanoporous Au-Pt. (b) 300 °C. (c) 400 °C. (d) 450 °C. (e) 500 °C. (f) 600 °C. Average ligament size L in each condition is presented. Note the difference in scale bars.

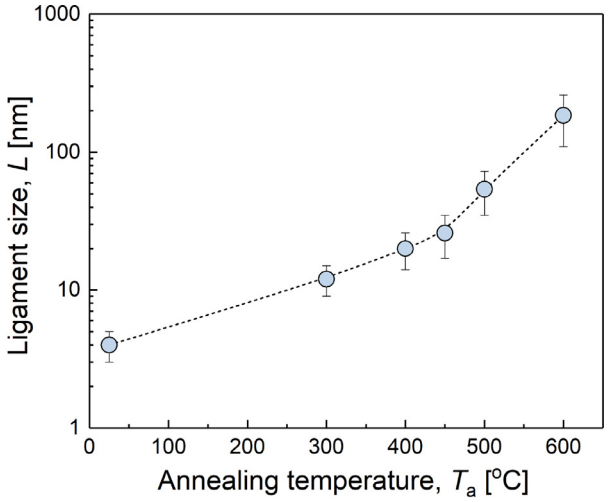

Fig. 2. Variation of ligament size, L, with annealing temperature, T_a. 25°C data point: as-dealloyed state.

position-sensitive solid-state detector. The data analysis used the procedures of [30]. In brief, Bragg reflections were fitted, individually or in groups, by split Pearson VII functions and the instrumental broadening corrected based on measurements of LaB_6 powder (NIST SRM 660b). Lattice parameters were refined by means of a Nelson-Riley-type approach with a correction for peak shifts due to stacking-faults [31,32]. Separating the contributions of coherent crystal size and of microstrain to the line broadening was based on Williamson-Hall analysis, assuming Cauchy size and Gaussian strain broadening [33,34].

3. Results

3.1. Ligament size

The microstructure of np Au-Pt in different conditions is apparent in the TEM images of Fig. 1. One perceives the nanoscale network structure that is well known for dealloyed nanoporous metals, yet here with the extremely small average size of 4 nm. After annealing at various temperatures, the ligament size increases and the porous structure remains uniform, as displayed in Figs. 1(b–f). The variation of the mean ligament size, L, with annealing temperature, T_a, is shown in Fig. 2. It is seen that L increases threefold (to 12 nm) already after the first annealing step, at 300 °C. L continues to increase with increasing T_a, reaching 185 nm after the 600 °C annealing.

3.2. Crystal structure

The crystal structure evolution of np Au-Pt during annealing is revealed by the X-ray diffraction patterns of Fig. 3. The as-dealloyed specimen (marked by 25 °C) exhibits a single fcc structure, as shown in Fig. 3(a). Similar crystal structure was also reported in other nanostructured Au-Pt systems [9,21,24]. Only fcc Au-Pt solid solution phases are observed. That observation is representative for our entire study, and specifically none of our experiments – X-ray or TEM – detected the γ(Pt-Ag) intermetallic phase [35]. The single set of fcc reflections prevails until peak splitting becomes apparent after annealing at 450°C. The interval of scattering angles, 2θ, between 60° and 90° is magnified in Fig. 3(b). The shoulder in the 220-reflection of that figure's 400°C graph implies that noticeable unmixing starts already at that annealing step.

After annealing at 450 °C, each peak has split, with the stronger component at lower angle. When the annealing temperature increases, that stronger component shifts towards the standard pattern of Au, whereas the weaker one shifts to that of Pt.

3.3. Element distribution

The element distribution in np Au-Pt was analyzed by EDS, and representative results are shown in Fig. 4. The EDS data suggests a uniform distribution of Au and Pt throughout the bulk of the as-dealloyed specimen (overlay of Au and Pt in Fig. 4(a)), demonstrating a nanostructured Au-Pt solid solution after dealloying. The EDS also reveals 10 ± 5 at.% Ag, where the error bars denote scat-

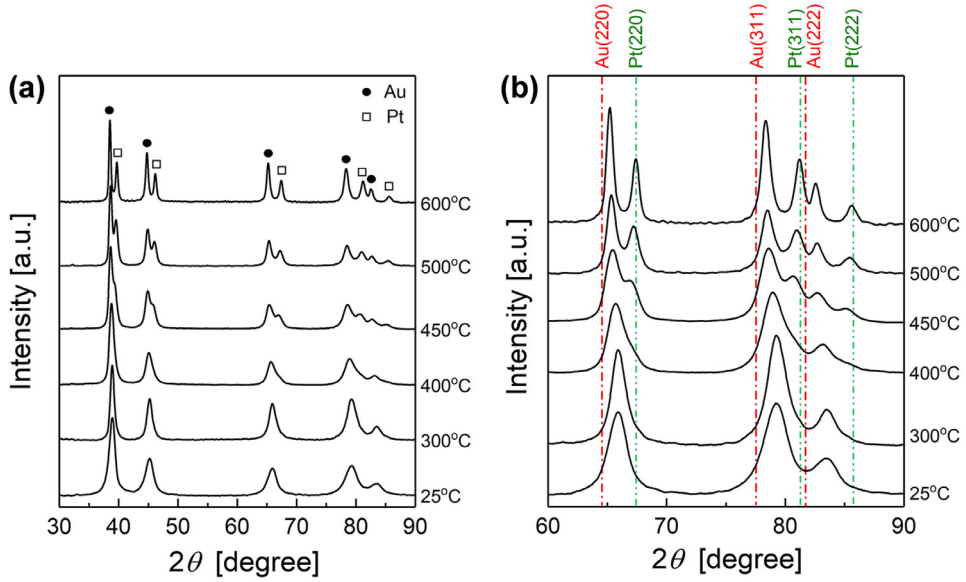

Fig. 3. X-ray powder diffraction. (a) Overview diffraction patterns of scattering intensity versus scattering angle 2θ. Reflections of face-centered cubic Au-rich and Pt-rich phases are labeled. (b) Details of scattering in interval $60° \leq 2\theta \leq 90°$. Red and green vertical lines: standard diffraction patterns of elemental Au (JCPDS 04-0784) and Pt (JCPDS 04-0802), respectively. 25°C scans: as-dealloyed state. (For interpretation of the references to color in this figure legend, the reader is referred to the web version of this article.)

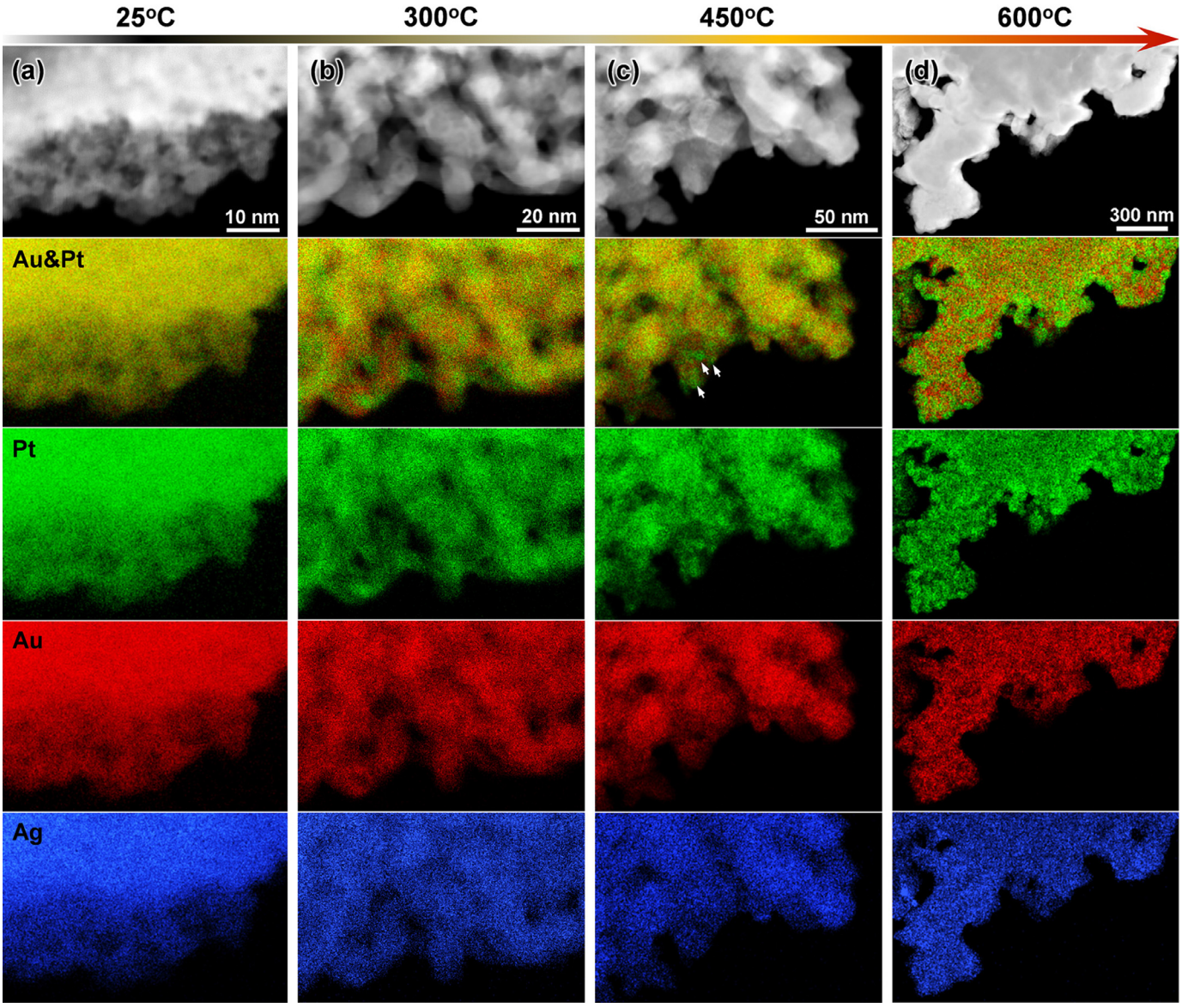

Fig. 4. Element-resolved transmission electron microscopy. Columns: micrographs of nanoporous Au-Pt (a) in as prepared state (labeled "25°C") and isothermally annealed at (b) 300 °C, (c) 450 °C and (d) 600 °C. From top row to bottom row: high-angle annular dark-field (HAADF) images, corresponding superimposed elemental maps of Au and Pt, Pt (green) chemical maps, Au (red) chemical maps, Ag (blue) chemical maps. Note the difference in scale bars for different annealing stages. (For interpretation of the references to color in this figure legend, the reader is referred to the web version of this article.)

ter over all samples of this study. The fraction of residual Ag agrees with earlier observations of Ag-Au-Pt dealloying in reference [8].

For the specimen annealed at 300 °C (Fig. 4(b)), the microscopy shows incipient unmixing. That is remarkable since the X-ray diffraction pattern in that state still suggests a single-phase structure. The Pt- and Au-rich domains have irregular shapes and appear to form a bicontinuous structure. The specimen annealed at 450 °C (Fig. 4(c)) exhibits a similar microstructure. Apart from the irregular domains, a few equiaxed Pt-rich particles are here observed, as indicated by arrows. After annealing at 600 °C, most of the Pt-rich regions tend to be equiaxed and randomly arranged in Au-rich ligaments (Fig. 4(d)).

Close inspection of Ag distribution in annealed specimen is displayed in Fig. 5. The residual Ag tends to aggregate in Au-rich regions, as revealed by the overlay of Au, Pt and Ag in Fig. 5(b). Four Pt-rich particles are marked out by arrows in Figs. 5(b-e). In those regions, a high Pt fraction correlates with low Au and low Ag.

The atom fractions of Au, Pt and Ag in Au-rich regions and Pt-rich regions measured by EDS are plotted as a function of annealing temperature, as shown in Fig. 6. Note that regions overlap along the electron beam path, so that each measurement will necessarily intermix signals from both types of regions. Therefore, we expect the true composition difference between the regions to be larger than what the EDS spectra indicate. All the data were measured in thin regions (e.g. near the edge of a ligament) to reduce the overlap and thus minimize the error. Each point in Fig. 6 represents the average of the measurements in at least ten positions.

In the as-dealloyed specimen (the 25 °C data point) with homogenous element distribution, the atom fractions of Au and Pt are almost equal. After annealing, the fractions of Au and Ag in Au-rich region gradually increase and the fraction of Pt decreases with increasing temperature, as indicated by the points on the solid lines. The compositions of the two types of regions in specimens annealed at the temperatures ranging from 300 °C to 450 °C

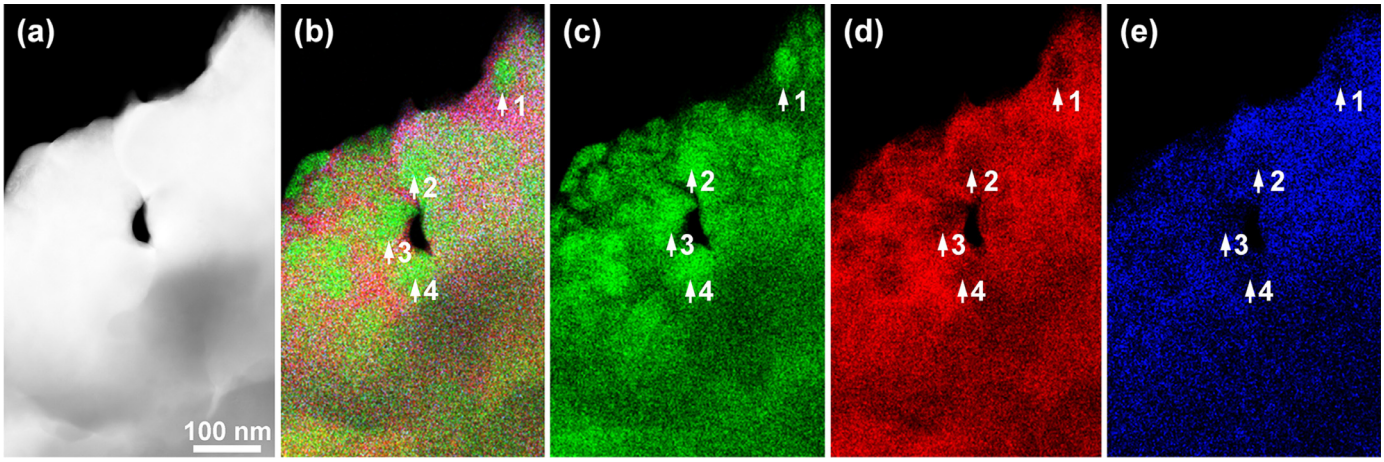

Fig. 5. Magnified TEM micrographs of nanoporous Au-Pt isothermally annealed at 600 °C. (a) High-angle annular dark-field (HAADF) image. (b) Corresponding superimposed elemental maps of Au, Pt and Ag. (c) Pt (green) chemical map. (d) Au (red) chemical map. (e) Ag (blue) chemical map. (For interpretation of the references to color in this figure legend, the reader is referred to the web version of this article.)

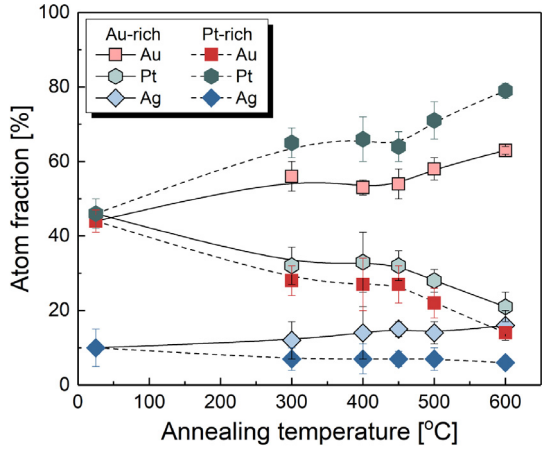

Fig. 6. Energy-dispersive spectroscopy results for atom fractions in Au-rich and Pt-rich regions versus annealing temperature. Open symbols linked by solid lines: Au-rich regions. Closed symbols linked by dashed lines: Pt-rich regions. Each data point represents an average over measurements at least 10 positions; error bars indicate standard deviation. 25°C data points: as-dealloyed state.

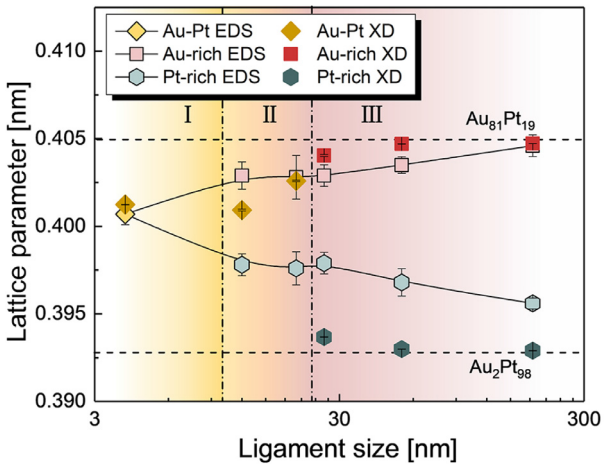

Fig. 7. Lattice parameters of Au-Pt, Au-rich and Pt-rich phases versus ligament size. Closed, unconnected symbols: results from X-ray diffraction (XD). Open symbols linked by solid lines: estimated based on energy-dispersive spectroscopy (EDS) and Vegards' law. Dashed horizontal lines: estimated lattice parameters of bulk terminal solid solutions at equilibrium at 600°C [12]. Roman numerals denote separate parts of the graph, as discussed in the main text.

are close, yet even higher temperatures bring an enhanced composition difference. The fraction of Au in Au-rich region reaches 60 at.% when the specimen is annealed at 600 °C, and the fractions of Pt and Ag are 21 at.% and 19 at.%, respectively. In comparison, the fraction of Pt in Pt-rich region is much higher than the fraction of Au in Au-rich region in the same annealing condition, and the former one reaches 80 at.% after annealing at 600 °C.

The difference of the composition between Au-rich and Pt-rich regions reflects the equilibrium alloy phase diagrams, where the solubilities of Pt and Ag in Au are indeed substantially higher than the solubility of Au or Ag in Pt [12,35,36]. In view of the lever rule, our observation of a larger volume fraction of Au-rich region is also consistent with the phase diagrams. As a result, after high temperature annealing, the Au-rich Bragg reflections have a larger area (Fig. 3), and the Pt-rich regions form isolated particles distributed in the continuous Au-rich matrix (Fig. 4).

3.4. Lattice parameters

Since the lattice parameters of Au-Pt solid solutions are well approximated by Vegard's law [12], their values may be estimated based on the EDS-compositions of Au-rich and Pt-rich regions of Fig. 6. As a consistency check, Fig. 7 compares that data to the X-ray lattice parameters. The estimate includes the residual Ag; note that the Ag lattice parameter is nearly identical to that of Au (lattice mismatch 0.17%). That is, the lattice parameter of the Au-Pt-Ag solid solution was computed as $a = a_{Au}(1 - x_{Pt}) + a_{Pt}x_{Pt}$, where x_{Pt} is the atom fraction of Pt documented in Fig. 6, and $a_{Au} = 408$ pm, $a_{Pt} = 392$ pm are the literature values for the lattice parameters of pure Au and pure Pt, respectively [12].

The plot in Fig. 7 can be divided to three parts. Part I is for the as-dealloyed state, ligament size 4 nm. Here, the lattice parameters estimated based on the EDS and directly measured by the X-ray diffraction agree. This is consistent with a homogeneous solid solution state in part I. Part II groups the states annealed at 300 °C and 400 °C, with ligament sizes ranging from 12 nm to 20 nm. Here, the EDS results reveal a two-phase system, while only one phase is detected by X-ray diffraction. The apparent disagreement calls for a closer inspection with high-resolution TEM, see below. The specimens annealed at 450–600 °C, with the ligament sizes > 26 nm, are grouped in part III. Here, two separate phases are detected by both approaches. Yet, the X-ray and TEM-based lattice

parameters differ, especially for the Pt-rich phase. It is plausible that the overlap of Pt-rich and Au-rich regions leads to error in the EDS composition, explaining the smaller lattice mismatch for the EDS results. The measurement error of composition should be larger for the small Pt-rich particles, as they tend to be covered by thick Au-rich matrix regions. This explains the deviation in this part of the graph.

Overall, the lattice parameters of the two phases do tend to converge towards what is expected based on the equilibrium phase diagram as the decomposition proceeds. Specifically, at the highest annealing temperature, the X-ray lattice parameters agree quite precisely with what is predicted (dashed lines in Fig. 7) by the alloy phase diagram combined with Vegard's law.

An obvious hypothesis explaining the inconsistency between the EDS and X-ray diffraction results in part II is that the Au-rich and Pt-rich regions are coherent, leading to a single set of X-ray diffraction peaks. The two regions might also be semicoherent with a very small lattice mismatch, so that their peaks cannot be distinguished in X-ray diffraction patterns.

3.5. Crystallographic relationship

Next, we inspect the crystallography of the Pt-rich regions that precipitated during annealing. We start out by noting that nanoporous metals made by dealloying typically retain the crystal lattice of the master alloy. Grain sizes in the nanoporous material are typically in the order of tens of micron, much larger than the pore size [8,37–39]. Thus, nanocrystalline regions are not expected here. Of interest is in how far the two phases emerging from the decomposition remain crystallographically coherent.

Fig. 8 analyzes a region of the 300°C annealed sample, showing the HAADF image in its part (a). Similar to Fig. 4(b), both Au-rich and Pt-rich regions are observed in Fig. 8(b). The corresponding selected area electron diffraction (SAED) pattern in Fig. 8(c) shows a single crystal structure, in other words, the two phases have identical crystallographic orientation.

The highlighted area of Fig. 8(a) and (b) is displayed at higher magnification in Fig. 8(d) and (e). Those images, along with their high-resolution TEM image and its Fourier transform (Fig. 8(f)) further demonstrate that neighbouring Au-rich and Pt-rich regions have the same crystallographic orientation.

The intensity profile along the white dashed line with $< 200 >$ direction across the interface in Fig. 8(f) is displayed in Fig. 8(g) as an approach to the local {200} interplanar spacing in each region. The distance between 10 lattice planes for each region is measured for enhanced accuracy. The {200} interplanar spacings in Fig. 8(g) are identical, suggesting that the Au-rich and Pt-rich regions are coherent. This agrees well with the single lattice parameter in the X-ray diffraction data. Similar findings were obtained in other regions.

To understand the crystallographic evolution at higher temperatures, a similar TEM analysis for the specimen annealed at 500°C is shown in Fig. 9. We focus on an area containing both Au-rich and Pt-rich regions in Fig. 9(b). The corresponding SAED pattern in Fig. 9(c) also shows a single crystal structure, indicating that the identical crystallographic orientation between the two regions is maintained. In this state of the sample, the X-ray data in Fig. 7 suggests a relative lattice mismatch between the phases of 2.9%; that small difference could not be distinguished in the SAED pattern. The identical orientation of Au-rich and Pt-rich regions in this specimen is further confirmed by high-resolution TEM image (Fig. 9(e–f)).

The difference of the lattice parameters between the two regions is revealed by the intensity profile in Fig. 9(g). The ten times {111} interplanar spacings in Fig. 9(g), 2.33 nm and 2.26 nm for the Au-rich and Pt-rich regions, respectively, imply a lattice mismatch of about 3%, in good agreement with the X-ray diffraction data.

To summarize, the results in Figs. 3–9 suggest that the microstructure of the decomposed alloy contains Au(Pt,Ag) and Pt(Au,Ag) solid solutions with identical orientation. The respective domains start out coherent and with identical lattice parameters. Upon annealing, lattice parameters start to differ and evolve towards those of the equilibrium terminal solid solutions at the annealing temperature.

3.6. Coherency length and microstrain

We have investigated the issue of crystallographic coherency further by analyzing X-ray line broadening, using results for nanoporous gold [30] as a benchmark. Even though the grain size of dealloyed nanoporous metals is much larger than the ligament size, L, the loss of coherent lattice sites in the pores lead to reflection broadening that can be analyzed for L. Fig. 10(a) shows the Williamson-Hall coherent scattering length [33], D_{W-H}, versus L as determined from the TEM data of Fig. 1. Also shown is the benchmark data for nanoporous gold. It is seen, that the data for np Au-Pt in its as-prepared and 300°C annealed states is within the trend field of nanoporous gold. By contrast, D_{W-H} of the 400°C annealed sample is noticeably below the trend field. That reduction of the coherent scattering length suggests a loss of coherency as a consequence of precipitation, indication of semi-coherent interfaces between matrix and precipitates [40].

The Williamson-Hall analysis also supplies estimates for the root-mean-square microstrain, and this data is plotted versus D_{W-H} in Fig. 10(b). The data is consistently above the trend line for nanoporous gold. This can be understood as the consequence of the atomic size misfit in the random solid solutions. Strain fields at coherent or semi-coherent interfaces might further contribute.

3.7. Surface composition

We have used cyclic voltammetry for estimating the Pt and Au atom fractions at the surface. Fig. 11(a) shows cyclic voltammograms (CVs) of np Au-Pt in different conditions. The two desorption peaks in the cathodic (negative-going) branches of all graphs are consistent with oxygen desorption peaks for Pt and Au, respectively [8,9,41]. The Pt/Au peak area ratio against annealing temperature is shown in Fig. 11(b). The fractional occupancy of the surface sites for the two elements can be roughly estimated from the charges of oxygen desorption (obtained from oxygen desorption peak areas) and the converting factors (390 μC/cm^2 for Au and 420 μC/cm^2 for Pt) [42]. That data is also plotted in Fig. 11(b). The surface fraction ratio starts out at 4.6, suggesting that the surface is strongly enriched in Pt in the as prepared state. This is in agreement with reports for other nanostructured Au-Pt alloys [7–9,43]. The figure also shows that the ratio decreases strongly during annealing, reaching about 1.5 after annealing at the highest temperature. This implies that the surface Pt atom fraction in the 600°C annealed state approximates the equimolar composition of the bulk.

4. Discussion

4.1. Uniform solid solution after dealloying

As was pointed out in the introduction, Au-Pt with the nominal composition of our nanoporous system after dealloying is not miscible at equilibrium except at very high temperatures, far from those of the room-temperature dealloying process. What is more,

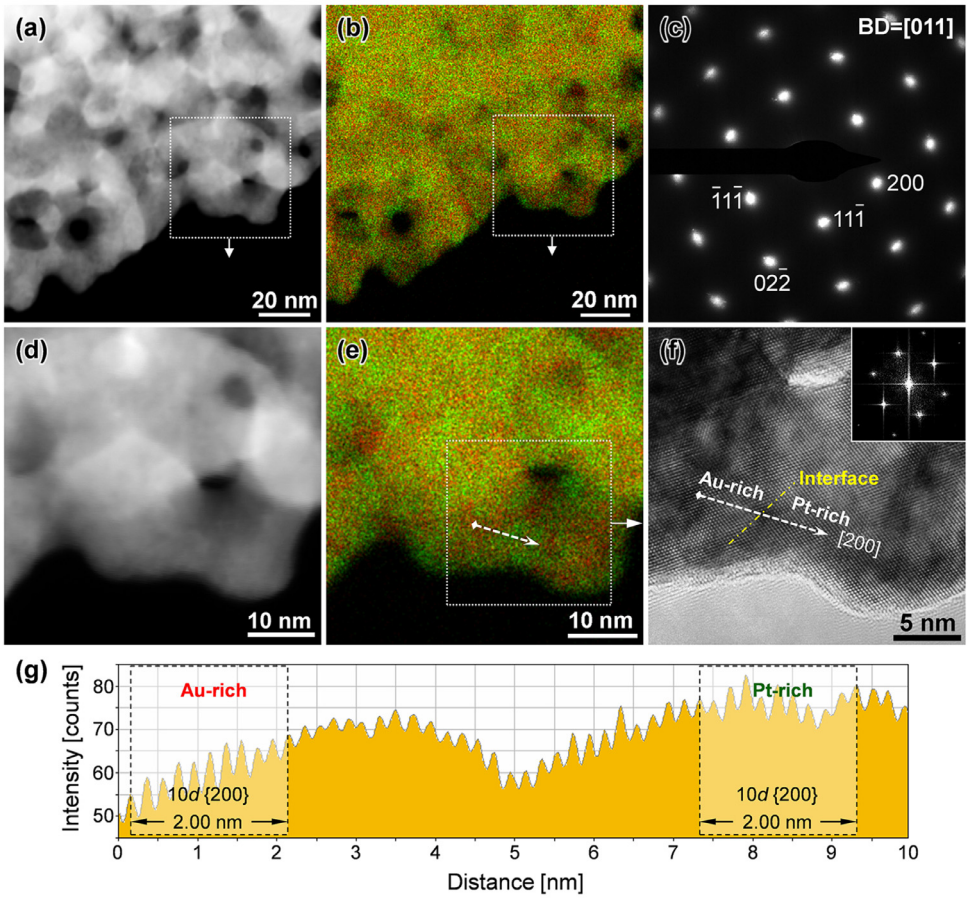

Fig. 8. TEM micrographs of nanoporous Au-Pt isothermally annealed at 300 °C. (a) High-angle annular dark-field (HAADF) image and corresponding (b) superimposed elemental maps of Au (red) and Pt (green). (c) Selected area electron diffraction pattern (SAED) along [011] zone axis corresponding to (b). (d) Magnification of the square area in (a). (e) Magnification of the square area in (b). (f) High resolution TEM image corresponding to the square area in (e). Fourier transform pattern is inserted. (g) The intensity profile along the dashed line across the interface in (f), revealing {200} interplanar spacing for each region. (For interpretation of the references to color in this figure legend, the reader is referred to the web version of this article.)

the alloy is within the region of spinodal instability in the alloy phase diagram. It is therefore remarkable that X-ray diffraction lattice parameters and TEM elemental maps consistently provide robust signatures for a uniform, single-phase solid solution in the bulk of the nanoporous material.

It is well established that the nanostructure formation during dealloying requires rearrangement of the more noble element (the component which is not corroded and forms the nanoporous product structure) at the scale of the ligament size. During aqueous dealloying, that rearrangement is carried by surface diffusion. The presence of substantial rearrangement suggests that the failure to decompose into the equilibrium phases cannot be explained by the mere lack of atomic mobility. Instead, one is led to suspect the presence of nucleation barriers.

Spinodal instability suggests pathways in configuration space for demixing that are free of nucleation barriers. Yet, coherency as well as confinement may act to suppress spinodal decomposition. With that in mind, we here present estimates of the upper convolute temperature, T_S, of the coherent spinodal and of the characteristic spinodal wavelength. The estimates are based on the following materials parameters: critical composition $x_C = 0.61$ and critical temperature of the equilibrium miscibility gap $T_C = 1260$°C [12]; Young's moduli $Y = 69$ and 140 GPa [44], Poisson's ratios $\nu = 0.42$ and 0.39 [45]. Furthermore, we took the composition-strain coupling parameter as $\eta = 2(a_{Au} - a_{Pt})/(a_{Au} + a_{Pt}) = 0.040$. As compared to the critical temperature, T_C, of the equilibrium phase diagram's miscibility gap, T_S in solids is lower by [46]

$$\Delta T_S = -\frac{1}{2R}\Omega\eta^2\frac{Y}{1-\nu} \tag{1}$$

where R and Ω denote the molar gas constant and the atomic volume, respectively. With the above materials parameters of the elements, and estimating the materials parameters of the solution at $x = x_C$ by composition-weighted linear interpolation, one obtains $\Delta T_S = 163$ K. In other words, the upper convolute temperature of the coherent spinodal is at ~ 1097°C, very much above room temperature. We conclude that coherency energy effects cannot explain a stabilization of the equimolar solid solution against spinodal decomposition at room temperature.

Next, we ask whether the decomposition may be suppressed because the spinodal wavelength is possibly much larger than the as-prepared ligament size. To this end, we approximate Au-Pt as a regular solution and obtain the solute-solute interaction energy parameter, ω, as $2RT_C$. Applying the equation for the fastest-growing wavelength, λ_m, in [47] to the regular solution, one has

$$q_m = \frac{1}{2^{2/3}}\sqrt{\frac{1-\tau}{\Omega^{2/3}}} \tag{2}$$

for the wave vector, $q_m = 2\pi/\lambda_m$, where $\tau = T/T_C$. This suggests that, within the temperature range of our dealloying and annealing experiments, λ_m varies between 2.9 nm (during dealloying at room temperature) and 4.3 nm (during annealing at the highest

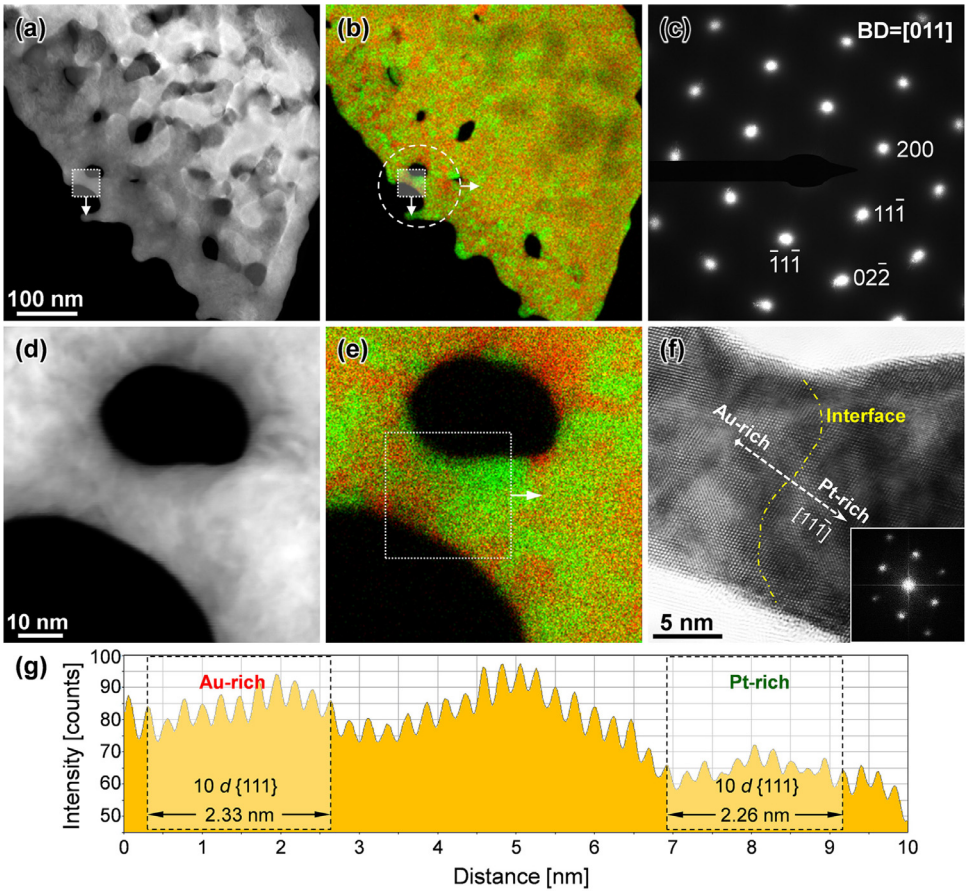

Fig. 9. TEM micrographs of nanoporous Au-Pt isothermally annealed at 500 °C. (a) High-angle annular dark-field (HAADF) image and corresponding (b) superimposed elemental maps of Au (red) and Pt (green). (c) Selected area electron diffraction pattern (SAED) along [011] zone axis corresponding to the circle in (b). (d) Magnification of the square area in (a). (e) Magnification of the square area in (b). (f) High resolution TEM image corresponding to the square area in (e). Fourier transform pattern is inserted. (g) The intensity profile along the dashed line across the interface in (f), revealing {111} interplanar spacing for each region. (For interpretation of the references to color in this figure legend, the reader is referred to the web version of this article.)

temperature, 600 °C). The as-prepared ligament size is already ∼ 4 nm, permitting more than a full spinodal wavelength within each ligament, even in the radial direction. We conclude that even the extremely fine structural length scale of our as-prepared np Au-Pt samples is not small enough for suppressing spinodal decomposition.

4.2. Role of residual silver

Our nanoporous material contains around 10 at.% of residual silver from the master alloy. It is therefore significant that the ternary Ag-Au-Pt alloy phase diagram [11] suggests that the binodals of the Au-rich and Pt-rich solid solutions shift only slightly when small fractions of Ag are added. Adding Ag displaces the miscibility gap slightly towards the Pt-rich side, and specifically the phase field of the Au-rich solution is widened. The small effect of Ag and the widening of the Au-rich solution's stability range are both qualitatively consistent with our discussion above.

4.3. Bulk depletion by surface segregation

As the spinodal decomposition is not observed in spite of the instability of the bulk solid solutions with the net composition of our alloy, we are led to investigate other decomposition modes. Here, it is relevant that the cyclic voltammetry points towards strong Pt enrichment at the surface. It is well-known that interface segregation in nanomaterials can substantially change the bulk composition, with important consequences for the stability of bulk phases [48–50]. We now present an estimate of the impact of the Pt enrichment at the surface for the Pt atom fraction in the bulk of our nanoporous alloy. We introduce surface and bulk site fractions, f_S and f_V with $f_S + f_V = 1$ and corresponding Pt atom fractions, x_S and x_V. Those atom fractions relate to the net platinum fraction in the alloy, x_{net}, by

$$x_S f_S + x_V f_V = x_{net} \tag{3}$$

The fraction of the surface sites relates to the ligament size through $f_S = \alpha\, d_{111}$. Here, α denotes the volume-specific surface area (area per volume of the solid phase) and d_{111} the interplanar spacing of the densest-packed crystallographic plane. By approximating the ligaments as cylinders, so that $\alpha = 4/L$, we obtain $f_S = 4d_{111}/L$. Thus, we estimate that 23% of all lattice sites in the as-prepared material ($L = 4$ nm) are surface sites. We note that the Pt/Au ratio at the surface as shown in Fig. 11(b) implies $x_S \approx 0.82$ in that state. This allows us to solve Eq. 3 for the bulk Pt fraction x_V in the as-prepared state. The result is $x_V = 0.35$. That bulk composition is outside of the chemical spinodal [12] and, thus, also outside of the coherent spinodal (which is the relevant one here).

The just-mentioned argument lets us conclude that the observed surface enrichment in Pt is sufficient for depleting the bulk of the ligaments in the as-prepared state in Pt, to an extent that moves the bulk out of the instable region of the phase diagram and into the metastable region between binodal and spinodal. During dealloying, the temperature is low and it is thus sensible to as-

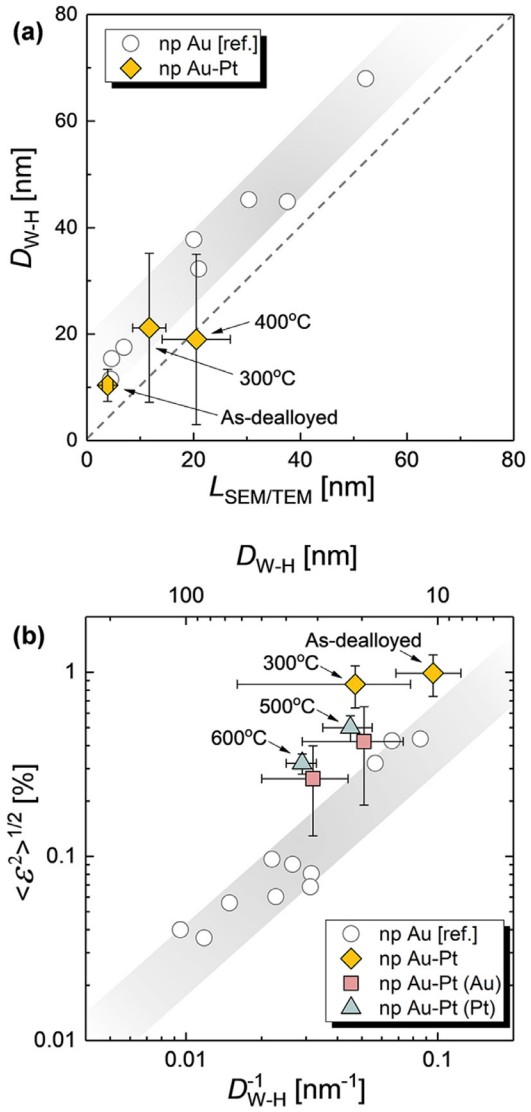

Fig. 10. Evaluation of the X-ray Bragg reflection broadening. (a) Williamson-Hall coherent scattering length, D_{W-H}, versus ligament size, L, derived from electron microscopy. Diamonds: nanoporous (np) Au-Pt, this work. Dashed: identity line. (b) Root-mean-square microstrain, $\langle\epsilon^2\rangle^{1/2}$, versus D_{W-H}. Colored symbols: nanoporous Au-Pt, analysis of single phase solid solution reflections (diamonds) and of separate reflection sets for Au-rich (squares) and Pt-rich (triangles) reflection sets. Open circles and shaded regions in (a) and (b): nanoporous gold, reference [30].

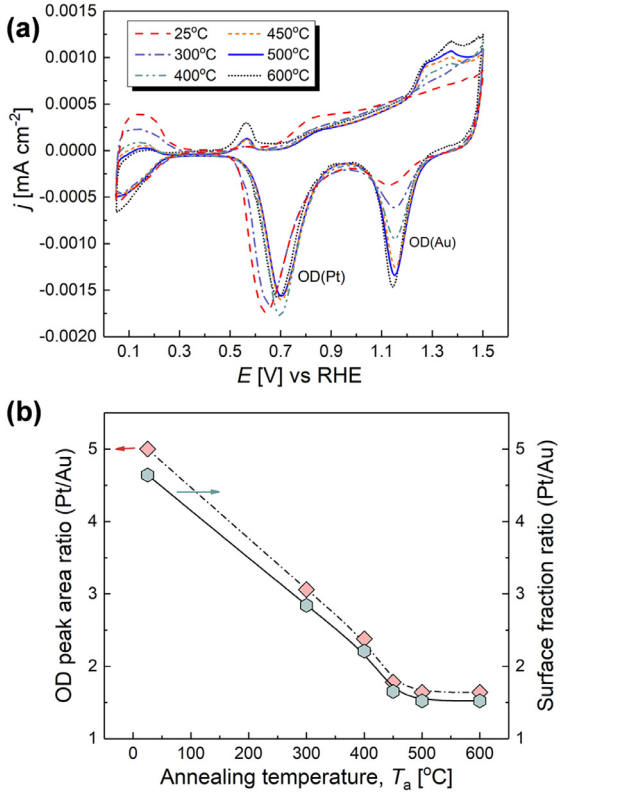

Fig. 11. (a) Cyclic voltammograms of current density j versus voltage E of nanoporous Au-Pt in different conditions. Electrolyte is 1 M $HClO_4$ solution and the scan rate is 1 mV/s. RHE means reversible hydrogen electrode. OH-desorption (OD) peaks for Pt and Au are marked out. (b) OD peak area ratio (diamonds linked by dashed line) and surface fraction (hexagons linked by solid lines) of Pt to Au versus annealing temperature. 25°C data: as-dealloyed state.

sume that nucleation of the Pt-rich phase in the bulk is kinetically suppressed.

When solute is found to be enriched at the surface of or at an internal interface in a solid solution, then the driving force is typically the heat of segregation, which energetically favors solute in surface sites. With increasing temperature, the entropy of mixing will start to dominate, and this typically diminishes the enrichment ratio, in other words, the local solid fractions in the surface and the bulk sites will approach a common value. Our observation of a reduced enrichment ratio with increasing annealing temperature is naturally compatible with that expectation, and it suggests an increased bulk Pt fraction in the annealed samples. That increase is further enhanced by the severe loss of surface sites that results from coarsening. Both factors thus cooperate in pushing Pt into the bulk, enhancing the driving force for the formation of Pt-rich regions. TEM and X-ray scattering results in our study demonstrate that process.

4.4. Microstructure evolution during annealing

Annealing of dealloyed nanoporous metals gives rise to curvature-driven, diffusion-mediated coarsening. We find L increasing threefold (from 4 nm to 12 nm) already at the lowest annealing temperature, 300 °C. As the volume of the surviving ligaments has increased $3^3 = 27$-fold, only about 4% of the initial ligaments have survived. With the possible exception of the 4% atoms in their core, every atom must have moved by distances in the order of the final ligament size. That is, the kinetics is sufficient for phase decomposition already after the lowest annealing step in our experiments. Yet, only an incipient signature of demixing is detected after the early stages of annealing. The aforementioned argument thus re-emphasizes that, during the early stages of annealing, the driving forces for the evolution of the composition field do not effciently push the system towards the equilibrium phases of the alloy phase diagram.

The apparently bicontinuous domain morphology after the 300°C anneal resembles that of early-stage spinodal decomposition. Yet, the decomposition pathway may here differ from classic spinodal decomposition. Data for Au self-diffusion [51] suggest the bulk diffusion coefficient $D = 1.6 \times 10^{-21}\mathrm{m}^2/\mathrm{s}$ at $T = 300°\mathrm{C}$. During the 1 h anneal, the diffusion distance is then $\sqrt{6Dt} \approx 6$ nm, so bulk diffusion can indeed contribute to the decomposition, on top of surface diffusion along the migrating surface. Yet, gradients in the mean curvature provide a separate driving force for microstructure evolution. Thus, the decomposition concurs with important coarsening. Incipient Au- or Pt-enriched regions will be dissolved when small ligaments vanish; these regions need to be reassembled at the surface of growing larger ligaments. In view of this frustrated

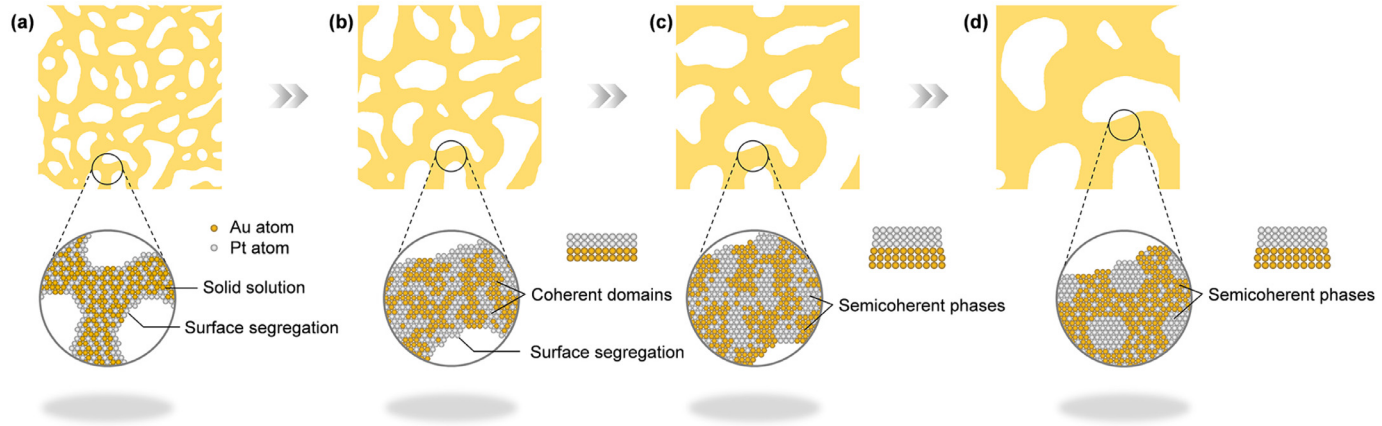

Fig. 12. Schematic illustration of phase decomposition in nanoporous Au-Pt.

unmixing situation, it is not surprising that the decomposition proceeds slowly.

Annealing at higher temperatures accelerates coarsening and phase decomposition, leading to the loss of coherency and the change in the phase morphology. The initially irregular Pt-rich regions evolve into more equiaxed ones which minimize the area of interface and thus reduced the net interfacial excess energy.

5. Summary

Our evaluation of the microstructure of as-dealloyed np Au-Pt and of its evolution during coarsening reveals that dealloying transforms the homogeneous, ternary bulk solid solution Ag-Au-Pt into a single-phase np Au-Pt solid solution. That solution would be immiscible at thermodynamic equilibrium, and its composition is within the alloy phase diagram's regime of spinodal instability. Upon annealing-induced coarsening, the initially single-phase solution evolves to a semicoherent two-phase state by way of an intermediate, coherent two-phase state. The findings for the formation and decomposition mechanisms can be summarized as follows (see also the schematics in Fig. 12 (a)–(d)):

(1) In the as-dealloyed state (Fig. 12(a)), surface segregation of Pt depletes the bulk of that element. Because of the extremely small ligament size and the many surfaces, the depletion is important enough to move the bulk composition into the metastable two-phase region of the alloy phase diagram, outside of the spinodal. Nucleation barriers for precipitation cannot be overcome at the low temperature of the dealloying, explaining why the bulk of the as-dealloyed material exhibits a uniform, single-phase state in spite of the substantial atomic rearrangements that accompany primary and secondary dealloying.

(2) Composition redistribution in np Au-Pt takes place upon annealing-induced coarsening. As the number of surface sites decreases, originally segregated Pt is pushed back into the bulk. The generic trend of segregation isotherms for surface enrichment factors to decrease in magnitude with increasing temperature provides a further driving force for the bulk Pt fraction to increase with increasing annealing temperature.

(3) In our sequence of annealing steps, the increase of the Pt-fraction in the bulk initially (up to ligament sizes of 12 nm) leads to crystallographically coherent Au-rich and Pt-rich regions (Fig. 12(b)). The phase morphology resembles that of early-stage spinodal decomposition, yet the unmixing is here frustrated, as it concurs with the dissolution of entire ligaments and the transport of their content to other, growing ligaments. The domains of different composition are then repeatedly dissolved and they have to reform elsewhere.

(4) Upon further coarsening, the fraction of Pt in surface sites decreases while that in the bulk continues to increase. The surface segregation of Pt becomes insubstantial after annealing at 450 °C. The initially coherent regions are now gradually replaced by semicoherent ones (Fig. 12(c and d)). That process accompanies an increase in the lattice mismatch. It goes along with a change in the phase morphology, the initially irregular shape of the Pt-rich regions evolving into more equiaxed ones that have minimized their area of interface and thus reduced the net interfacial excess energy.

Based on the formation and decomposition mechanisms above, nanostructured alloys with high kinetic stability and tunable surface composition can be designed. By appropriate annealing, the surface area and phase component can be tailored to obtain desired material properties.

Declaration of Competing Interest

The authors declare that they have no known competing financial interests or personal relationships that could have appeared to influence the work reported in this paper.

Acknowledgments

This work was supported by Deutsche Forschungsgemeinschaft (DFG) through Project 192346071, SFB 986.

References

[1] R. Newman, S. Corcoran, J. Erlebacher, M. Aziz, K. Sieradzki, Alloy corrosion, MRS Bull. 24 (7) (1999) 24–28.
[2] J. Erlebacher, M.J. Aziz, A. Karma, N. Dimitrov, K. Sieradzki, Evolution of nanoporosity in dealloying, Nature 410 (6827) (2001) 450–453.
[3] J. Weissmller, K. Sieradzki, Dealloyed nanoporous materials with interface-controlled behavior, MRS Bull. 43 (1) (2018) 14–19.
[4] F. Kertis, J. Snyder, L. Govada, S. Khurshid, N. Chayen, J. Erlebacher, Structure/processing relationships in the fabrication of nanoporous gold, JOM 62 (6) (2010) 50–56.
[5] M. Graf, B. Roschning, J. Weissmller, Nanoporous gold by alloy corrosion: method-structure-property relationships, J. Electrochem. Soc. 164 (4) (2017) C194–C200.
[6] X.-L. Ye, N. Lu, X.-J. Li, K. Du, J. Tan, H.-J. Jin, Primary and secondary dealloying of au(pt)-ag: structural and compositional evolutions, and volume shrinkage, J. Electrochem. Soc. 161 (12) (2014) C517–C526.
[7] J. Snyder, P. Asanithi, A.B. Dalton, J. Erlebacher, Stabilized nanoporous metals by dealloying ternary alloy precursors, Adv. Mater. 20 (2008) 4883–4886, doi:10.1002/adma.200702760.
[8] H.-j. Jin, X.-l. Wang, S. Parida, K. Wang, M. Seo, J. Weissmüller, Nanoporous Au-Pt alloys as large strain electrochemical actuators, Nano Lett. 10 (2010) 187–194, doi:10.1021/nl903262b.
[9] C. Xu, R. Wang, M. Chen, Y. Zhang, Y. Ding, Dealloying to nanoporous Au/Pt alloys and their structure sensitive electrocatalytic properties, Phys. Chem. Chem. Phys. 12 (2010) 239–246, doi:10.1039/b917788d.

[10] A.A. Vega, R.C. Newman, Nanoporous metals fabricated through electrochemical dealloying of ag-au-pt with systematic variation of Au:Pt ratio, J. Electrochem. Soc. 161 (1) (2013) C1–C10.
[11] A. Prince, Ag-Au-Pt (Silver - Gold - Platinum); in Landolt-Brnstein - Group IV Physical Chemistry -Noble Metal Systems. Selected Systems from Ag-Al-Zn to Rh-Ru-Sc, 11B, Springer-Verlag, Heidelberg, 2006, doi:10.1007/10916070_7. https://materials.springer.com/lb/docs/sm_lbs_978-3-540-46994-0_7
[12] H. Okamoto, T. Massalski, The Au-Pt (Gold-Platinum) system, Bull. Alloy Phase Diagr. 6 (1) (1985) 46–56, doi:10.1007/BF02871187.
[13] R.W. Carpenter, Growth of modulated structure in gold-platinum alloys, Acta Metall. 15 (10) (1967) 1567–1572.
[14] Y. Zeng, B. Gaskey, E. Benn, I. McCue, G. Greenidge, K. Livi, X. Zhang, J. Jiang, J. Elebacher, Electrochemical dealloying with simultaneous phase separation, Acta Mater. 171 (2019) 8–17, doi:10.1016/j.actamat.2019.03.039.
[15] J. Erlebacher, An atomistic description of dealloying – porosity evolution, the critical potential, and rate-limiting behavior, J. Electrochem. Soc. 151 (10) (2004) C614–C626.
[16] K. Binder, Spinodal decomposition in confined geometry, J. Non-Equilib. Thermodyn. 23 (1998) 1–44, doi:10.1515/jnet.1998.23.1.1.
[17] R.A. Jones, L.J. Norton, E.J. Kramer, F.S. Bates, P. Wiltzius, Surface-directed spinodal decomposition, Phys. Rev. Lett. 66 (10) (1991) 1326–1329.
[18] H. Jinnai, H. Kitagishi, K. Hamano, Y. Nishikawa, M. Takahashi, Effect of confinement on phase-separation processes in a polymer blend observed by laser scanning confocal microscopy, Phys. Rev. E – Stat. Phys. Plasmas Fluids Relat. Interdiscip. Top. 67 (2) (2003) 7, doi:10.1103/PhysRevE.67.021801.
[19] R.W. Balluffi, J.W. Cahn, Mechanism for diffusion induced grain boundary migration, Acta Metall. 29 (3) (1981) 493–500.
[20] A. King, Diffusion induced grain boundary migration, Int. Mater. Rev. 32 (1) (1987) 173–189.
[21] S. Zhou, G.S. Jackson, B. Eichhorn, AuPt alloy nanoparticles for CO-tolerant hydrogen activation: architectural effects in Au-Pt bimetallic nanocatalysts, Adv. Funct. Mater. 17 (2007) 3099–3104, doi:10.1002/adfm.200700216.
[22] J.K. Lee, J. Lee, J. Han, T.-H. Lim, Y.-E. Sung, Y. Tak, Influence of au contents of AuPt anode catalyst on the performance of direct formic acid fuel cell, Electrochim. Acta 53 (9) (2008) 3474–3478.
[23] J. Zeng, J. Yang, J.Y. Lee, W. Zhou, Preparation of carbon-supported core- shell au- pt nanoparticles for methanol oxidation reaction: the promotional effect of the au core, J. Phys. Chem. B 110 (48) (2006) 24606–24611.
[24] P.N. Njoki, J. Luo, L. Wang, M.M. Maye, H. Quaizar, C.-J. Zhong, Platinum-catalyzed synthesis of water-soluble gold-platinum nanoparticles, Langmuir 21 (2005) 1623–1628.
[25] Y.C. Lu, Z. Xu, H.A. Gasteiger, S. Chen, K. Hamad-Schifferli, Y. Shao-Horn, Platinum-gold nanoparticles: a highly active bifunctional electrocatalyst for rechargeable lithium-air batteries, J. Am. Chem. Soc. 132 (2010) 12170–12171, doi:10.1021/ja1036572.
[26] X. Zhou, R. Darvishi Kamachali, B.L. Boyce, B.G. Clark, D. Raabe, G.B. Thompson, Spinodal decomposition in nanocrystalline alloys, Acta Mater 215 (2021) 117054, doi:10.1016/j.actamat.2021.117054.
[27] X. Ge, X. Yan, R. Wang, F. Tian, Y. Ding, Tailoring the structure and property of pt-decorated nanoporous gold by thermal annealing, J. Phys. Chem. C 113 (17) (2009) 7379–7384, doi:10.1021/jp9008702.
[28] A. El-Zoka, B. Langelier, G. Botton, R. Newman, Morphological evolution of Pt-modified nanoporous gold after thermal coarsening in reductive and oxidative environments, npj Mater. Degrad. 4 (40) (2020) 1–6, doi:10.1038/s41529-020-00143-4.
[29] A.A. Vega, R.C. Newman, Beneficial effects of adsorbate-induced surface segregation of Pt in nanoporous metals fabricated by dealloying of Ag-Au-Pt alloys, J. Electrochem. Soc. 161 (1) (2014) C11–C19, doi:10.1149/2.014401jes.
[30] M. Graf, B.-n.D. Ngô, J. Weissmüller, J. Markmann, X-ray studies of nanoporous gold: powder diffraction by large crystals with small holes, Phys. Rev. Mater. 1 (2017) 076003, doi:10.1103/PhysRevMaterials.1.076003.
[31] J. Markmann, P. Bunzel, H. Rosner, K.W. Liu, K.A. Padmanabhan, R. Birringer, H. Gleiter, J. Weissmüller, Microstructure evolution during rolling of inert-gas condensed palladium, Scr. Mater. 49 (7) (2003) 637–644.
[32] J. Markmann, D. Bachurin, L. Shao, P. Gumbsch, J. Weissmüller, Microstrain in nanocrystalline solids under load by virtual diffraction, Epl 89 (6) (2010) 66002.
[33] H. Klug, L. Alexander, X-Ray Diffraction Procedures, Wiley, New York, 1974.
[34] J. Markmann, V. Yamakov, J. Weissmller, Validating grain size analysis from x-ray line broadening: a virtual experiment, Scr. Mater. 59 (1) (2008) 15–18.
[35] I. Karakaya, W. Thompson, The Ag-Pt (Silver-Platinum) system, Bull. Alloy Phase Diagr. 8 (4) (1987) 334–340, doi:10.1007/BF02869269.
[36] H. Okamoto, T. Massalski, The Ag-Au (Silver-Gold) system, Bull. Alloy Phase Diagr. 4 (1) (1983) 30–38, doi:10.1007/BF02881183.
[37] S. Parida, D. Kramer, C.A. Volkert, H. Rsner, J. Erlebacher, J. Weissmller, Volume change during the formation of nanoporous gold by dealloying, Phys. Rev. Lett. 97 (3) (2006) 035504.
[38] H.J. Jin, L. Kurmanaeva, J. Schmauch, H. Rösner, Y. Ivanisenko, J. Weissmüller, Deforming nanoporous metal: role of lattice coherency, Acta Mater. 57 (2009) 2665–2672, doi:10.1016/j.actamat.2009.02.017.
[39] S.V. Petegem, S. Brandstetter, R. Maass, A.M. Hodge, B.S. El-dasher, J. Biener, B. Schmitt, C. Borca, H.V. Swygenhoven, On the microstructure of nanoporous gold: an X-ray diffraction study, Nano Lett. 9 (3) (2009) 1158–1163.
[40] D.A. Porter, K.E. Easterling, M.Y. Sherif, Phase Transformations in Metals and Alloys, third ed., Taylor & Francis Group, New York, 2014.
[41] M. Breiter, Electrochemical characterization of the surface composition of heterogeneous platinum-gold alloys, J. Phys. Chem. 69 (3) (1965) 901–904, doi:10.1021/j100887a033.
[42] S. Trasatti, O. Peterii, Real surface area measurements in electrochemistry, Pure Appl. Chem. 63 (5) (1991) 711–734.
[43] A.F. Ebrahimy, B. Langelier, R.C. Newman, Atom probe tomography of nanoporous gold formed by dealloying lean noble alloys, Mater. Today Commun. 25 (2020) 10137, doi:10.1016/j.mtcomm.2020.101371.
[44] M. Salvadori, I. Brown, A. Vaz, L. Melo, M. Cattani, Measurement of the elastic modulus of nanostructured gold and platinum thin films, Phys. Rev. B – Condensed Matter Mater.Phys. 67 (2003) 153404, doi:10.1103/PhysRevB.67.153404.
[45] W. Köster, H. Franz, Poisson's ratio for metals and alloys, Metall. Rev. 6 (1) (1961) 1–56, doi:10.1179/mtlr.1961.6.1.1.
[46] J.W. Cahn, On spinodal decomposition, Acta Metall. 9 (1961) 795–801.
[47] J.W. Cahn, Phase separation by spinodal decomposition in isotropic systems, J Chem Phys 42 (1) (1965) 93–99.
[48] J. Weissmller, Alloy effects in nanostructures, Nanostruct. Mater. 3 (1–6) (1993) 261–272.
[49] J. Weissmüller, H. Ehrhardt, Segregation-induced instability of nanocrystalline line compounds, Phys. Rev. Lett. 81 (5) (1998) 1114–1117.
[50] H.A. Murdoch, C.A. Schuh, Stability of binary nanocrystalline alloys against grain growth and phase separation, Acta Mater. 61 (6) (2013) 2121–2132.
[51] W. Rupp, U. Ermert, R. Sizmann, Self-diffusion measurements in gold single crystals between 286 and 412°c, Phys. Status Solidi (b) 33 (2) (1969) 509–516.